

Article

Alkali-Activated Materials with Pre-Treated Municipal Solid Waste Incinerator Bottom Ash

Yoleimy Avila , Rui Vasco Silva *  and Jorge de Brito 

Civil Engineering Research & Innovation for Sustainability (CERIS), Instituto Superior Técnico, Universidade de Lisboa, Av. Rovisco Pais, 1049-001 Lisboa, Portugal; yoleimy.pereira@tecnico.ulisboa.pt (Y.A.); jrb@civil.ist.utl.pt (J.d.B.)

* Correspondence: rui.v.silva@tecnico.ulisboa.pt

Abstract: This study presents the results of an experimental campaign on the use of municipal solid waste incinerator bottom ash (MIBA) and fly ash (FA) as precursors for the production of alkali-activated materials. MIBA was subjected to a pre-treatment stage in response to two issues: high metallic aluminum content, which reacts in a high pH solution, releasing hydrogen; and low amorphous content of silica-, aluminum- and calcium-bearing phases, which translates into a limited formation of reaction products. The proposed pre-treatment stage oxidizes most of the metallic aluminum fraction and compensates for the low reactivity of the material via the formation of additional reactants. Different combinations of MIBA and FA were tried—mass-based ratios of 0/100, 25/75, 50/50, 75/25, and 100/0 for MIBA/FA. Two mix designs of the alkaline activator with sodium hydroxide and sodium silicate were evaluated by varying the Na_2O /binder and $\text{SiO}_2/\text{Na}_2\text{O}$ ratios. These mortars were tested in the fresh and hardened state. The results showed that the pre-treatment stage was effective at stabilizing the dimensional variation of MIBA. Despite the lower reactivity of MIBA, mortars with 50/50 of MIBA/FA presented a maximum 28-day compressive strength of 25.2 MPa, higher than the 5.7 MPa of mortars made with MIBA only.

Keywords: alkali-activated materials; municipal solid waste incinerator bottom ash; fly ash; pre-treatment



Citation: Avila, Y.; Silva, R.V.; de Brito, J. Alkali-Activated Materials with Pre-Treated Municipal Solid Waste Incinerator Bottom Ash. *Appl. Sci.* **2022**, *12*, 3535. <https://doi.org/10.3390/app12073535>

Academic Editor: Jong Wan Hu

Received: 11 February 2022

Accepted: 26 March 2022

Published: 30 March 2022

Publisher's Note: MDPI stays neutral with regard to jurisdictional claims in published maps and institutional affiliations.



Copyright: © 2022 by the authors. Licensee MDPI, Basel, Switzerland. This article is an open access article distributed under the terms and conditions of the Creative Commons Attribution (CC BY) license (<https://creativecommons.org/licenses/by/4.0/>).

1. Introduction

According to the International Labour Organization (ILO), essential services are globally understood as those that, if interrupted, lead to a clear and imminent threat to life, personal safety, or health of the whole or part of the population [1]. Although this concept of essentiality has become popular due to the COVID-19 pandemic, giving rise to subjectivities associated with each country and their circumstances [2], an objective and global reality is that the collection of domestic waste is an essential activity that fits perfectly within the guideline defined by the ILO [3].

In 2019, the generation of municipal solid waste (MSW) in the European Union (EU) increased around 1% compared to 2018, which the production of an additional 2 million tonnes [4]. This value was expected to be significantly higher in 2020, considering the numerous quarantines and working from home due to the pandemic, which caused an increase of 6.9% in the 27 EU State Members in 2020 when compared to 2019 (from 5.5% to 12.4%) [5] and could imply a greater amount of waste was generated and disposed of.

This upward trend in the amount of generated MSW, also directly associated with population growth [6], raises the importance of the research on the technical feasibility of the waste streams generated from the combustion of solid waste [3,7,8]. This process is carried out in order to reduce between 70% and 90% of the volume of domestic waste collected, while its combustion is used to produce energy [9].

One of the sub-products generated in this procedure corresponds to MIBA [10,11], which has been studied as a precursor of alkali-activated materials (AAM); these types of materials are manufactured by mixing a precursor rich in amorphous aluminosilicates and

calcium with an alkaline solution [12–14], providing mechanical and durability properties similar or even greater to those of conventional Portland cement composites [15]. These relatively new bound construction materials are considered more sustainable from the use of industrial wastes as raw materials.

Although MIBA shows pozzolanicity, which makes it a viable precursor in this type of reaction [16–18], most researchers agree that this material has two main weaknesses: the presence of metallic aluminum that reacts with the alkaline solution to produce hydrogen gas (i.e., on average 1360 mL H₂/g of Al is generated [19]); and low content of amorphous aluminosilicates, in comparison with other precursors such as ground-granulated blast-furnace slag (GBFS), FA or metakaolin, which do not require improvement stages to achieve AAM with an excellent performance [20–23].

To solve the aluminum issue, Joseph et al. [24] proposed in their research a pre-treatment stage, which consisted of immersing MIBA in water, with a liquid/solid ratio of 5/1, and placing it in an oven at 105 °C for 24 h. With increasing temperature, the reaction rate between the aluminum and water releases all the H₂. Huang et al. [25] proposed a uniform agitation for 4 h of the NaOH solution and the MIBA in order to release all the H₂ possible. These same authors replaced 40% of MIBA for granulated blast furnace slag (GBFS) to improve the mechanical properties.

Regarding the low content of amorphous aluminosilicates, Maldonado-Alameda et al. [26] found a low quantity of reaction products from activated MIBA, thereby requiring aluminum or silicate correctors to achieve adequate performance. In their work, they used the 8 to 30 mm fraction of MIBA and PAVAL as a source of PV reactive aluminum, which is an industrial waste generated from the secondary aluminum recycling process. Their results showed a decline in the mechanical properties because of the resulting high porosity and decreased compressive strength from 25.6 to 12.1 MPa. Cristelo et al. [27] evaluated the combination of MIBA with FA, in order to improve the mechanical performance, obtaining specimens that were dimensionally more stable than the others made with MIBA alone as a precursor. Wongsu et al. [28] evaluated the effect of replacing 0%, 20%, and 40% of type C FA with MIBA, obtaining a compressive strength of 45.6 MPa with a replacement of 40% compared to a strength of 10.6 MPa at 28 days for MIBA-only composites. Finally, Huang et al. [29] proposed heat treating of MIBA at different temperatures prior to the grinding stage (350, 700, and 1050 °C) to remove the organic content and improve the content of amorphous aluminosilicates, and a hydrogen release stage, making the NaOH solution react for 3 h with MIBA before the calcination stage.

Other studies have been developed to assess the inclusion of secondary wastes as precursors of AAM together with other well-known precursors. Wang et al. [30] replaced up to 25% of alkali-activated slag with fluorogypsum and up to 15% with flue-gas desulfurization gypsum. The first waste precursor corresponds to the residue generated from the production of hydrochloric acid and the second is a residue of desulfurization of thermal plants. In this research it was concluded that the sulphate ions present in the gypsum can lead to the formation of ettringite, which caused a rupture in the pastes with increasing contents. Yurt and Bekar [31] produced alkali-activated concrete using replacements of 0%, 5%, 10%, and 15% of hazelnut shell biomass ash and metakaolin as replacements of GBFS as the main precursor. The addition of both materials led to an improvement in the compressive strength. Lima et al. [32] studied the performance of alkali-activated GBFS using coffee husk ash as the secondary precursor. The results showed that the mix made with both precursors presented better mechanical behavior than that of the control sample. Different investigations have been carried out on the use of MIBA as a precursor of AAM, in which several methodologies were proposed to mitigate the effect of the reaction of metallic aluminum with the alkaline activator on dimensional stability. Other studies evaluated strategies to improve the concentration of the amorphous phases with the purpose of obtaining a better mechanical performance, but few studies have developed a proposal with an approach that includes the two weaknesses of the precursor.

This work shows the results of an experimental campaign whose objective was focused on proposing a methodology to improve the two weaknesses of MIBA, as mentioned above.

During this procedure, replacements were used of pre-treated MIBA by FA type F of 0%, 25%, 50%, 75%, and 100%, together with two alkaline activator designs: optimal alkaline activator (OAA) and constant alkaline activator (CAA). The pre-treatment MIBA stage consisted of mixing with the NaOH solution, the heat of which was released by the reaction of dissolving NaOH in water and was used to accelerate the oxidation of aluminum in the fresh state, and subsequently a resting time of 24 h was allowed. Different properties in the fresh and hardened state were evaluated in the monolithic material.

2. Materials and Methods

2.1. Precursors

MIBA sampling was carried out in the Valorsul facility, in São João da Talha, Portugal. The collected sample for this experimental campaign corresponds to the residue generated in the month of January 2019. Before the grinding stage of MIBA, there was an initial preparation that included drying at 105 °C and manual cleaning in order to remove the plastic, wood, and metallic particles. Grinding was divided into three stages: grinding in a Los Angeles device for 30 min; crushing the fraction with a particle size greater than 4 mm in a cylinder mill; and finally crushing of all the material for two hours in a large ball mill. FA was supplied by EDP—Gestão da Produção de Energia, S.A.—at the Sines power plant.

2.2. Alkaline Activator and Water Reducing Admixtures

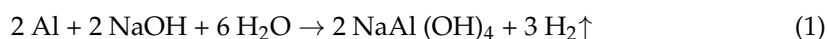
Sodium hydroxide pellets, with 98% purity and a density of 2.13 g/mL, and sodium silicate solution with 26.4 ± 1.5% of SiO₂, 8 ± 0.6% of Na₂O and 65.6 ± 2% of water were used. Tap water from the public network of EPAL company, complying with Directive 98/83/CE [33], was used in the preparation of the alkaline activator. SikaPlast-717 was used as a water-reducing admixture (WRA), which contains naphthalene-based superplasticizer for commercial use, and consists of a combination of synthetic organic water-based dispersants, with a density of 1.21 ± 0.03 kg/dm³, chloride ion content ≤ 0.1 %, and a pH of 10 ± 1. Such WRA usually contains naphthalene, sulfuric acid, formalin, and alkali [34].

2.3. Aggregates

According to standard EN 12620 [35], two types of siliceous sand from Sesimbra, Portugal, were used as aggregate: 0/4 coarse sand and 0/1 fine sand.

2.4. Pre-Treatment MIBA

AAM with MIBA as precursor required 24 h of contact with the sodium hydroxide solution in order for the hydroxyl ion (OH⁻) to react with the metallic aluminum present in this type of waste. This allows the hydrogen gas to be released, while the mix is fresh. The main chemical reaction that takes place in the pre-treatment is the following:



In the present research, the heat released in the reaction of dissolving NaOH in water was used as catalyst for the release of hydrogen (46.2 kJ/mol at a NaOH concentration of 1 mol/L). A higher concentration of alkali will catalyze the reaction of metallic aluminum due to increased heat input [24]. Rosenband and Gany [36] studied the behavior of the release of hydrogen associated with the reaction of aluminum with water at different temperatures; they observed that, when the water reached 74 °C, the reaction occurred in a shorter time than when they used water at 50 °C.

The alkaline solution was prepared by dissolving the amount of NaOH solute in the tap water solvent. Then, this solution was quickly added to the previously weighed MIBA together with the WRA, acting as a dispersant and particle-wetting surfactant, and stirred for 10 min. After that, the fresh mix was poured into a container, covered with a plastic lid with several holes at the top, where it rested for 24 h.

2.5. Mix Design

The viability of the precursor's composition was assessed based on a substitution of 0% (0.0 M), 25% (0.25 M), 50% (0.5 M), 75% (0.75 M), and 100% (1.0 M) of pre-treated MIBA with FA. The binder/aggregate volumetric ratio (V_B/V_A) was defined as 0.33 and the water/binder volumetric ratio (V_W/V_B) was fixed at 0.4. The total amount of water in this ratio corresponds to that from the sodium silicate solution and from the added tap water. A mass ratio WRA/binder of 1% was applied, excluding the 0.0 M mix.

The production and preparation of mortars were carried out in accordance with EN 196-1 [37], adapted to AAM production; specifically the general requirements for the equipment: mixer, molds, spreaders, and jolting apparatus, in addition to the compaction procedure (number of layers and jolts). Once pre-treatment MIBA was carried out, the evaporated water was compensated, and this precursor was homogenized for 5 min in the mixer bowl. Then the FA was added, and mixing proceeded for 5 more minutes. Later, sodium silicate was placed and mixed for 5 min and, finally, the aggregates were poured with a mixing time of 5 min.

Once the molding of the mortars was complete, they remained for a period of 24 h in ambient conditions, covered by a plastic film, and were subsequently placed in the oven at 80 °C for 24 h. After this time, the specimens were stripped and sealed with a plastic film until the day of the test.

Two ratios were defined for NaOH and Na₂SiO₃ in the design of the alkaline activator; the first was Na₂O/binder, where the numerator corresponds to the sum of the contributions of Na₂O from sodium hydroxide and sodium silicate and the denominator corresponds to FA + MIBA. The second ratio was SiO₂/Na₂O, wherein the numerator comes entirely from the sodium silicate solution and the denominator corresponds to the Na₂O in the previous ratio. A preliminary study determined that the optimal ratios, at 28 days of curing of Na₂O/binder and SiO₂/Na₂O for FA (0.0 M) and MIBA (1.0 M), corresponded to 15/1.0 and 8/0, respectively. The first design of the activator, named the optimal alkaline activator (OAA), was established from the optimal ratio based on the proportionality of each precursor. For the 0.0 M mix, the values for the Na₂O/binder and SiO₂/Na₂O ratios were 15% and 1 (15/1), respectively, and for the 1.0 M mix they were 8% and 0 (8/0). For 0.25 M, the ratio used was 13.25/0.75; for 50% MIBA (0.5 M) it was 11.5/0.5 and for 75% MIBA (0.75 M) it was 9.75/0.25. The second design of the alkaline activator, named the constant alkaline activator (CAA), consisted in defining the average ratio of 11.5/0.5 for all proportions of precursors. Tables 1 and 2 present the contents used for each mix according to the alkaline activator design.

Table 1. Composition of alkali-activated mortars with OAA (g/dm³).

MIX	MIBA	FA	WRA	Water	NaOH	Na ₂ SiO ₃	Fine Sand	Coarse Sand
1.0 M	514.31	0.00	5.14	210.11	55.44	0.00	452.01	1050.66
0.75 M	398.56	127.21	5.26	175.69	61.79	49.06	447.20	1039.49
0.5 M	262.68	251.53	5.14	130.45	66.15	114.43	442.12	1027.67
0.25 M	129.64	372.40	5.02	74.80	68.51	195.19	436.38	1014.34
0.0 M	0.00	491.34	0.00	9.47	69.22	291.55	431.82	1003.74

Table 2. Composition of alkali activated mortars with CAA (g/dm³).

MIX	MIBA	FA	SP	Water	NaOH	Na ₂ SiO ₃	Fine Sand	Coarse Sand
1.0 M	524.87	0.00	5.25	130.32	66.08	114.32	441.70	1026.70
0.75 M	393.84	125.70	5.20	130.39	66.11	114.37	441.91	1027.18
0.5 M	262.68	251.53	5.14	130.45	66.15	114.43	442.12	1027.67
0.25 M	131.40	377.47	5.09	130.51	66.18	114.48	442.33	1028.16
0.0 M	0.00	505.64	0.00	131.12	66.49	115.01	444.39	1032.95

2.6. Test Methods

The chemical composition of MIBA and FA was quantified by X-ray fluorescence (XRF), using an S4 Pioneer apparatus of Bruker (Cordoba, Spain), with a potential of 4 kV. Similarly, the crystalline phases present in the precursors were determined by X-ray diffraction (XRD) using a Bruker D8 Discover A25 instrument with Cu-K α radiation (Cordoba, Spain). The particle size of both binders was characterized by laser diffraction using a Malvern Instruments Mastersizer laser diffraction particle size analyzer (Cordoba, Spain) with a 99% pure ethanol as dispersant, and its density measurements were carried using Sievert PCT-Pro 2000 (Spain). The aluminum content in MIBA was quantified through the capture of hydrogen generated by the chemical reaction of the metallic element with a NaOH solution. Finally, the hydrogen potential (pH) was tested for both materials using a HACH brand digital pH measurement instrument (Lisbon, Portugal) according to the standard ASTM D4972 [38].

The aggregates' particle size distribution test was carried out according to EN 933-1 [39]. The density and water absorption tests were carried out according to EN 1097-6 [40]. The consistency of mortar mixes in the fresh state was evaluated based on the flow table test described in EN 1015-3 [41]. The bulk density was carried out according to EN 1015-6 [42]. The compressive and flexural strengths were measured according to EN 1015-11 [43], the dry bulk density according to EN 1015-10 [44], and the dynamic modulus of elasticity as per EN 14146 [45]. These properties were evaluated at 7, 28, 91, and 182 days of age. In addition, shrinkage according to EN 1015-13 [46], water absorption by capillary action according to EN 1015-18 [47], water absorption by immersion described in LNEC E394 [48], and carbonation depth according to EN 13295 [49] were evaluated for mixes made with the CAA design.

3. Results and Discussion

3.1. Characterization of the Precursors

Table 3 shows the chemical composition of the MIBA and of the FA used. The data show that the sum of the oxides SiO₂ + Al₂O₃ + Fe₂O₃ corresponds to 88.7% and 64.3% for FA and MIBA, respectively. When comparing these values with those of ASTM C618-5 [50], it is possible to classify FA as type F, in which the sum of the oxides has a minimum established value of 70%. In the case of MIBA, the classification as per ASTM indicates that the waste can be classified as a type C ash, since the value exceeds the established limit of 50% for the sum of the oxides. According to the literature, 66% of MIBAs comply with this limit [51].

Table 3. Chemical composition of raw materials, FA, and MIBA (% by mass).

Materials	FA (%)	MIBA (%)
Al ₂ O ₃	25.55	8.85
CaO	2.28	18.33
Fe ₂ O ₃	6.92	6.69
K ₂ O	2.75	1.59
MgO	1.83	4.02
Na ₂ O	1.30	6.55
SiO ₂	56.44	48.92
SO ₃	0.80	1.36
Cl ⁻	0.00	0.00
Cr ₂ O ₃	0.49	0.06
TiO ₂	1.14	0.48
ZnO	0.02	0.35
P ₂ O ₅	0.44	2.52
V ₂ O ₅	0.05	-
CuO	0.00	0.16
MnO ₂	-	0.12

Figure 1 corresponds to the XRD results of the MIBA samples used in the present study. The crystalline phases observed are quartz (SiO_2), calcite (CaCO_3), magnetite ($\text{Fe}^{2+}\text{Fe}^{3+}_2\text{O}_4$), fayalite ($(\text{Fe}^{2+})_2\text{SiO}_4$), magnesite (MgCO_3), microcline (KAlSi_3O_8), magnesium phosphate ($\text{Mg}_3(\text{PO}_4)_2$), sodium calcium iron phosphate, and anhydrite (CaSO_4). These results are consistent with those of other research works where similar minerals were found for MIBA [52,53]. The crystalline phases observed for FA, showed on the same figure, are quartz (SiO_2), lime (CaO), maghemite ($\text{Fe}^{3+}_2\text{O}_3$), and mullite. The mineralogical characterization of FA is similar to that reported by other authors [21,54].

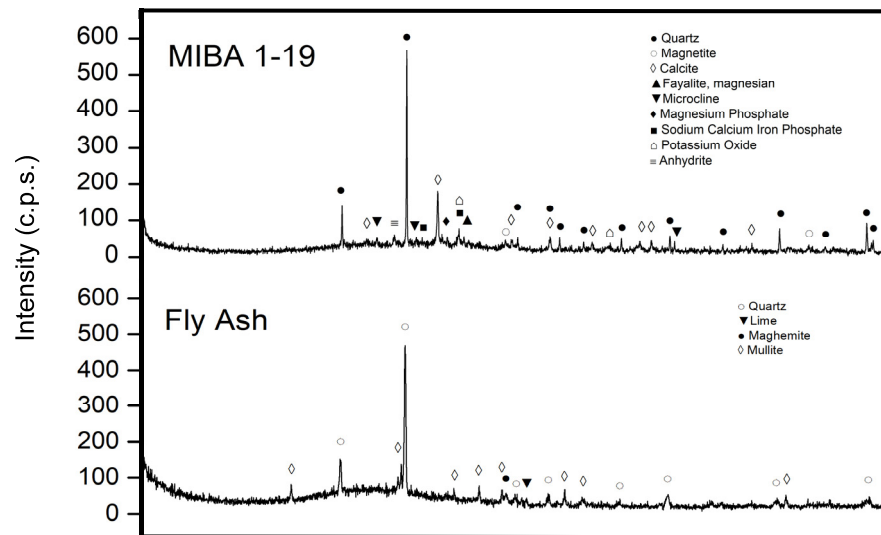
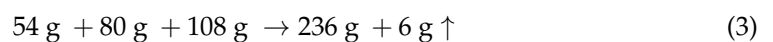


Figure 1. XRD pattern of FA and MIBA.

The amount of released hydrogen from MIBA was calibrated using a method involving the reaction of pure aluminum particles. The chemical reaction to produce gaseous hydrogen from metallic aluminum and sodium hydroxide corresponds to Equation (2). Stoichiometric quantities (atomic and molecular weights in grams) are presented in Equation (3).



From the stoichiometric quantities, it was determined that 0.11 g of $\text{H}_2 \uparrow$ was produced per gram of aluminum consumed (Equation (4)).

$$\text{g H}_2 \uparrow = 1 \text{ g Al}^0 \times \frac{6 \text{ g H}_2 \uparrow}{54 \text{ g Al}^0} = 0.11 \text{ g} \quad (4)$$

From the reaction of 0.1 g of metallic aluminum with a 2.5 M NaOH solution (excess reagent), the volume of water displaced by the hydrogen gas produced was measured experimentally in an inverted test tube, which was connected through a glass tube to a three-nozzle balloon (Figure 2). The theoretical value from Equation (2) corresponds to 143.03 mL of H_2 gas. Three trials were carried out to determine the average experimental value and calculate the error as a function of the theoretical value. The temperature at which the reaction was carried out was 43 °C. This heat was due to the exothermic reaction of NaOH in water. The density of the hydrogen at 43 °C and 1 atm. of pressure is 0.0766 kg/m³ [55]. From this property and the mass of hydrogen produced by each gram of aluminum (Equation (5)), it was possible to determine the theoretical volume of hydrogen generated.

$$v = \frac{m}{\rho}; v_{\text{H}_2} = \text{ / mL} = 1436.03 \text{ mL} \quad (5)$$



Figure 2. Experimental setup of quantification of metallic aluminum in MIBA.

One gram of metallic aluminum generates 1.436 L of H_2 . To quantify the metallic aluminum in MIBA, the test was carried out with 30 g of this precursor and 800 mL of a 2.5 M NaOH solution. Using the density, the milligrams of hydrogen present in 158.7 mL of the gas were determined as follows (Equation (6)):

$$v \times \rho = m; 158.67 \text{ mL} \times 0.0000766 \frac{\text{g}}{\text{mL}} = 0.01215 \text{ g} = 12.15 \text{ mg} \quad (6)$$

where v corresponds to the volume in mL, ρ is the density in g/mL and m , the mass in mg. Using the stoichiometry weights, in Equation (7), the amount of metallic aluminum that produces this quantity of hydrogen was determined.

$$\text{g Al}^\circ = 0.01215 \text{ g H}_2 \uparrow \times \frac{54 \text{ g Al}^\circ}{6 \text{ g H}_2 \uparrow} = 0.1640 \text{ g Al} \quad (7)$$

Therefore, in 30 g of MIBA there are ~164 mg of metallic aluminum, and it can be concluded that there are 5.46 g of Al/kg of MIBA, and that this aluminum in contact with an excess NaOH solution produces 7.91 L of $H_2 \uparrow$ /kg of MIBA.

Laser diffraction particle size analysis was carried out to determine the particle size distribution of MIBA, after the grinding stage, and FA. Figure 3a,b shows the particle size distribution in MIBA and FA, respectively. A share of 90% of the MIBA distribution varied from 0.5 to 120 μm and 90% of the FA distribution varied from 1 to 110 μm . The densities and pH of precursors were, for FA, 2.425 g/cm³ and 10.70, respectively, and, for MIBA, were 2.704 g/cm³ and 9.50.

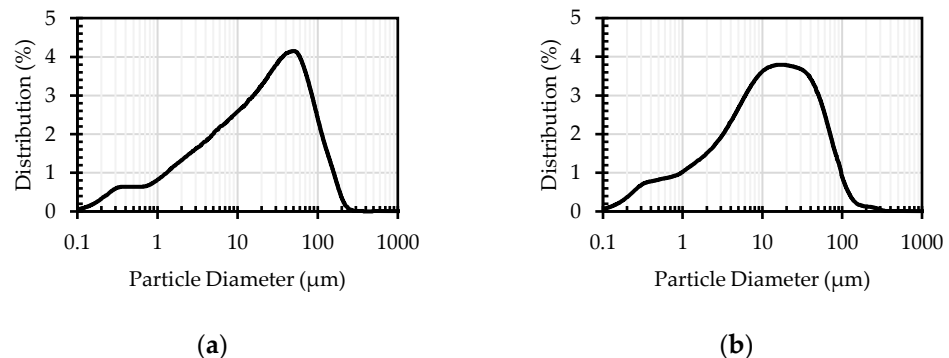


Figure 3. Particle size distribution: (a) MIBA (b) FA.

3.2. Characterization of the Aggregates

The dried density was determined as 2620 kg/m³ for fine sand 0/1 and 2610 kg/m³ for coarse sand 0/4. The water absorption of the fine sand 0/1 and coarse sand 0/4 was 0.2%

and 0.3%, respectively. Figure 4 shows the aggregates' particle size distribution. Fine sand 0/1 varies from 2 to 0.0625 mm, whereas the coarse sand 0/4 varies from 8 to 0.0625 mm. They present a D_{max} of 1 and 4 mm, respectively.

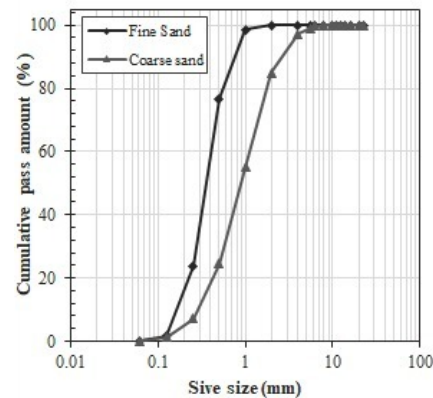


Figure 4. Particle size distribution of aggregates.

3.3. MIBA Pre-Treatment

In the pre-treatment, MIBA was mixed with a solution containing the amount of NaOH needed for each mix. For the OAA design, the concentration of hydroxyl ion increased with decreasing MIBA content (Figure 5a).

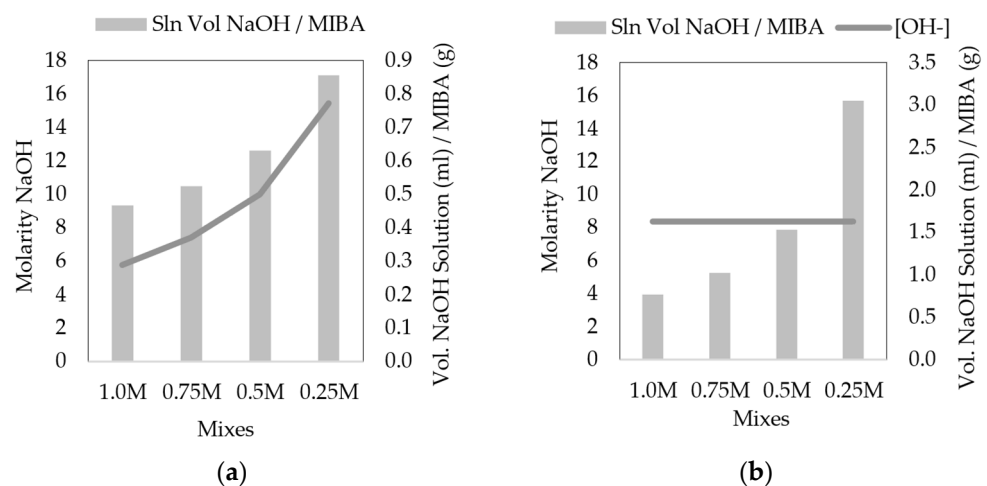


Figure 5. Concentration and volume of the alkaline solution in the pre-treatment of MIBA: (a) OAA design and (b) CAA design.

Hence, the elimination of aluminum for mixes with a lower content of this precursor will be more efficient. For the CAA design, the OH^- concentration in the pre-treatment stage was the same for all mixes: 8.37 M (Figure 5b). With increasing ratio between the NaOH solution and the MIBA mass, it is expected that the oxidation reaction of metallic aluminum will be more efficient in the mixes with lower MIBA content.

3.4. Fresh-State Properties

3.4.1. Consistency

The workability of the mixes was evaluated using the flow table test (EN 1015-3 [41]). The flow values determined for the mixes in the fresh state with OAA and CAA are presented in Figure 6a,b, respectively. As expected, workability improved with increasing FA content. This is due to the well-known spherical shape of its particles, which reduced interparticle friction. An increase of 54% in consistency was observed for the 1.0M CAA mix when compared to that of the corresponding OAA mix. This is likely due to the

effectiveness of the CAA design pre-treatment (i.e., greater Na_2O content than in the OAA design) in eliminating the existing aluminum particles. This was observed in other mixes with MIBA.

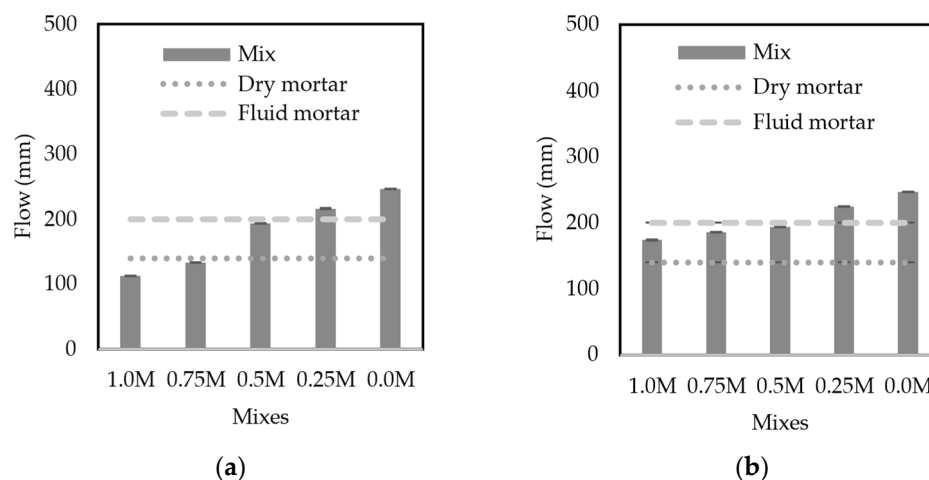


Figure 6. Flow values of: (a) OAA mixes and (b) CAA mixes.

The results reported in this study are in accordance with other studies. Among these, Das et al. [56] determined the workability of alkali-activated concrete mixes using type F FA as precursor, incorporating low amounts of lime and silica lime as a replacement for the FA. They reported a decrease in slump with a decreasing amount of FA. Other authors [57] observed that, when increasing the amount of magnesium ferronickel slag, along with a decrease in the amount of type F FA in alkali-activated pastes, the fluidity decreased. Indeed, the high workability granted by FA is due to the spherical morphology of its particles, which reduces the viscosity of the fresh mixes by reducing interparticle friction [58].

Regarding the effect of WRA used in this study, it has a working mechanism similar to that of lignosulfonate-based WRA, providing an electrical dispersion effect [59], inducing changes in the solid–liquid interface, which improves the workability. Topçu and Ateşin [34] reported in their research that mixes with naphthalene-based dispersants presented greater slump flow diameters when compared to mixes with lignosulfonate-based dispersants. Burgos-Montes et al. [60] studied the compatibility between WRA and cement with mineral additions. These authors concluded that FA exhibits greater affinity to melamine- and naphthalene-based admixtures than the other mineral additions used in that study. They explained the improved performance as a result of the morphology of the particles, which favored polymeric adsorption.

3.4.2. Density

The determination of bulk density in the fresh state was carried out according to EN 1015-6 [42], whereas that property in the hardened state was determined according to EN 1015-10 [44]. Figure 7a,b show the density in the fresh state and in the hardened state at 28 days of the mixes made with the OAA and CAA designs, respectively. It is relevant to point out the discrepancy between the fresh vs. hardened state density of the mortars. The latter is usually lower than the former due to the evaporation of the mixing water throughout the curing period. This difference is greater for mixes with higher MIBA content and more notable for the OAA design. This is due to the lower effectiveness of the corresponding pre-treatment, which left a greater amount of unreacted aluminum particles that produced hydrogen in the mortar production stage. The presence of H_2 -filled pockets in the fresh mix led to lower density values. For the mixes with the OAA design (Figure 7a), the density in the fresh state varied between 1.90 and 2.27 g/cm^3 and it increased with increasing FA content. Although MIBA is denser than FA, the latter may present greater compacity due to their morphology. Moreover, the density of MIBA-containing mixes is

also lower, probably due to the aforementioned phenomenon. Residual aluminum particles release H₂ gas when in contact with Na₂SiO₃, leading to the foaming of the mortar [61]. The mixes with higher FA contents, by showing greater densities in the hardened state, will probably present better mechanical properties as they are more compact.

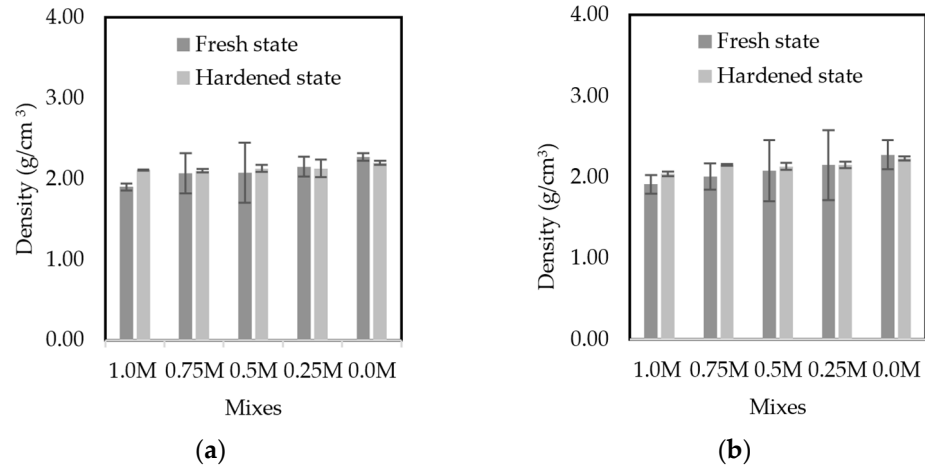


Figure 7. Fresh and hardened-state densities of: (a) OAA mixes and (b) CAA mixes.

3.5. Hardened-State Properties

3.5.1. Compressive Strength

Figure 8 shows the results of compressive strength at 7, 28, 91, and 182 days for the OAA and CAA mixes. The maximum 28-day compressive strength was that of the 100% FA mix: 61 and 39 MPa for the OAA and CAA designs, respectively. The minimum values were those of mixes with 100% MIBA; 5.36 and 5.72 MPa for the OAA and CAA designs, respectively. The 28-day and 182-day compressive strength values of the mixes with 50/50 of MIBA/FA were 19.8 and 25.2 MPa, respectively. Marginal strength development was observed in OAA mixes containing 25% FA in comparison with those without it (i.e., ~100% increase after 28 days).

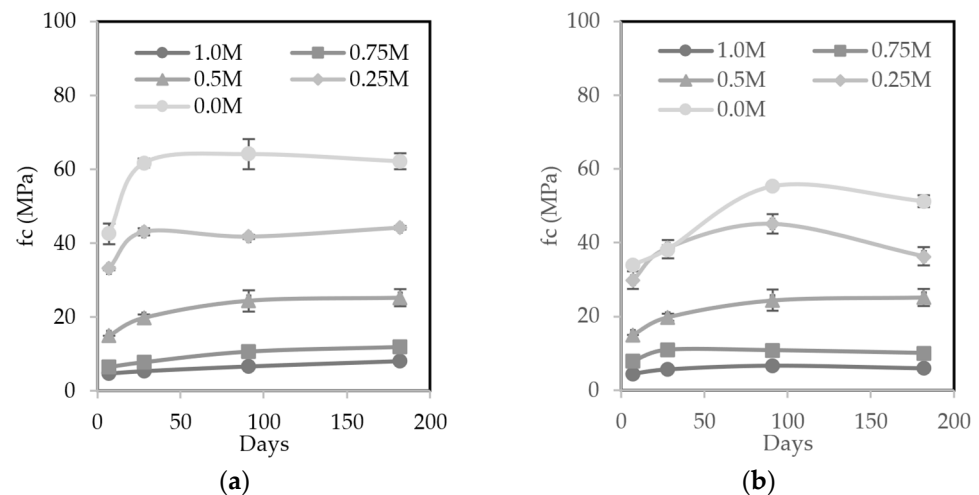


Figure 8. Compressive strength of: (a) OAA mortars and (b) CAA mortars.

For longer curing periods, the trend maintained regarding the mixes with the highest and lowest compressive strengths. This indicates that there is an enhanced strength development with increasing FA content. The crosslinking of the reaction product in the activation process of type F FA (a precursor characterized for its high content of Al and Si and a low content of Ca) is analyzed as a monolithic alkali-activated gel, which is not yet completely understood [62]. By comparison, MIBA is more similar to a precursor with

a high Ca content, where the main reaction products correspond to C-A-S-H gel and its structure is strongly associated with the activator used [63]. The type of gel that is formed when mixing FA and MIBA-like precursors will depend on the reaction mechanisms, which will be analyzed in subsequent studies. By mixing the two materials to obtain an AAM, the FA structure may function as a bound network that envelops the MIBA particles, which present low pozzolanic activity. This means that MIBA does not completely deteriorate the mechanical properties of the new material but reduces them proportionally to the percentage of addition. Other hypotheses about the reaction mechanism in which the MIBA particles are fixed in the structure formed by the alkaline activation of the FA consist of the previous formation of zeolites before gelation [64], where the smaller MIBA particles may be adsorbed in the pores generated by the zeolites produced from the hydrothermal conditions of the amorphous aluminosilicates present in the FA in highly basic solution (pH greater than 13) [15,65,66]. Moudar et al. [67] recently identified and characterized the zeolitic phases in the alkaline activation of FA type F, identifying the presence of amorphous metastable aluminosilicates, which are the intermediate phases in the formation of zeolites. Both hypotheses about the reaction mechanics between FA and MIBA will be clarified in upcoming stages of research. Wongsat et al. [28] studied mixes where type C FA was replaced with MIBA at 0%, 20%, 40%, and 100%. These authors concluded that the 20% and 40% replacement levels of FA with MIBA led to the highest compressive strengths (53 and 45.6 MPa, respectively, when compared with 42 MPa of the mix without MIBA; 100% MIBA exhibited a compressive strength of 10.6 MPa). The improved performance when adding MIBA may have been partly due to the greater presence of waste glass particles, which are known to actively contribute to the strength development of alkali-activated mixes.

In another study, Kuri et al. [57] studied binary mixes, where type F FA was replaced at 0%, 25%, 50%, 75%, and 100% with ferronickel magnesium slag. The alkaline activator used was a mix of NaOH and Na₂SiO₃, and two curing conditions were used: thermal curing at 60 °C for 24 h; and ambient curing. With thermal curing, when the content of ferronickel increased from 0% to 75%, the compressive strength increased from 33 to 45 MPa at 28 days of curing. However, for the AAM with 100% ferronickel slag, the compressive strength was substantially reduced to 16 MPa. Interestingly, the morphology presented by ferronickel slag is similar to that presented by MIBA, with both residues being very well coupled in the formation of a new material. In the study of Xie et al. [68], wherein different contents of FA with GBFS were combined, satisfactory results were observed in the manufacture of alkali-activated concrete with recycled aggregates. The authors observed that, as the slag content increased, the compressive strength increased, reaching values of 79.6 MPa for the largest replacements. The GBFS of this research had a calcium content of 35.05%, which may have led to a stronger interfacial transition zone (ITZ) between the aggregates and cement paste.

The compressive strength development was also evaluated for carbonated mortars made with the CAA design. To this end, 28 days after the sealed curing, the prismatic specimens were cured in a carbonation chamber (5% CO₂, 20 °C, and 60% RH) for 7, 14, and 28 days and their compressive strength determined at 35, 49, and 77 days, respectively, after their production. Figure 9 shows that the compressive strength of carbonated mortars was substantially higher than that of uncarbonated mortars. The highest relative increase in compressive strength due to carbonation occurred in mixes with the highest proportions of MIBA, as it is a precursor with relatively high calcium content. At 28 days after the accelerated carbonation curing, the compressive strength of the 1.0 M mix was 19.1 MPa, around 140% higher than the maximum value reported for the uncarbonated mix (8.08 MPa). For the 0.5 M mix, this increase was around 40%. For the 0.0 M mix, a compressive strength increase of 30% was observed after 28 days of carbonation. This enhanced performance is associated with the decalcification of Ca-bearing phases, which, reacting to the CO₂ dissolved in the pore solution, led to the precipitation of calcium carbonate (CaCO₃) in the capillary pores of the AAM matrix. This leads to an increase in densification and microstructural cohesion, and thus in compressive strength [16]. In the mix with 100% FA,

which is classified as type F, the formation of this product occurs but to a lesser extent due to the lower presence of Ca-bearing phases. However, a notable increase was nevertheless observed, inferring the existence of another strength-enhancing mechanism; this is likely related to the carbonation of Na^+ ions (already existing in the pore solution and from the desodification of N-A-S-H gels), leading to the formation of sodium carbonates and the greater polymerization of existing silicate chains [69].

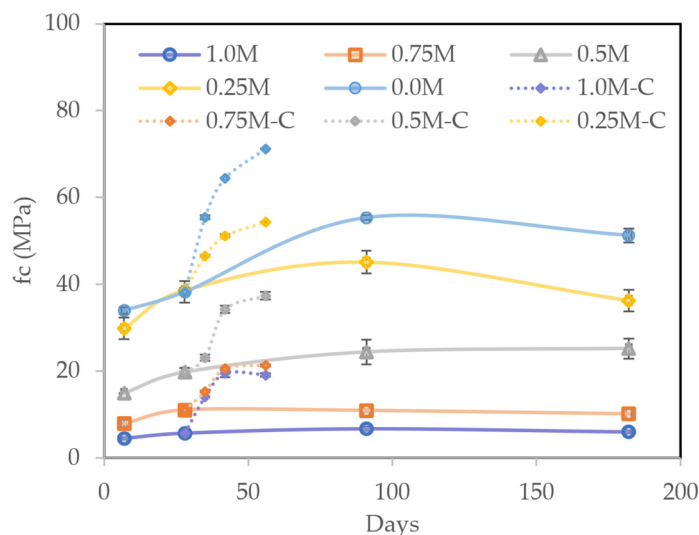


Figure 9. Compressive strength of uncarbonated and carbonated mortars with CAA design.

Regarding the carbonation depth itself, the phenolphthalein indicator test did not present any coloration, indicating that the matrix had a pH lower than 9 and thus presenting “complete carbonation” after 28 days in the carbonation chamber. Consequently, despite carbonation leading to an improvement in compressive strength, it is detrimental to AAM if applied in steel-reinforced structures [70].

3.5.2. Flexural Strength

Figure 10 shows the flexural strength results at 7, 28, 91, and 182 days for the mixes made with the OAA and CAA designs. As observed for compressive strength, the maximum flexural strength values were obtained for the mix with 100% FA and the minimum values for the mix with 100% MIBA. This trend is maintained over time. The 0.0 M mix produced with the CAA design presents a much lower flexural strength than those made with the OAA design. The higher amount of Na_2O from NaOH in the latter led to the increased pH of the activator, which improved the dissolution of the amorphous aluminosilicate FA particles. Concerning the 0.25 M mixes, despite the lower amount of Na_2O in the CAA method, mixes using this method presented a higher flexural strength when compared with OAA mixes. This suggests that the $\text{Na}_2\text{O}/\text{binder}$ and $\text{SiO}_2/\text{Na}_2\text{O}$ ratios’ calibration is not linear depending on the proportionality of the precursors.

Figure 11 shows that the flexural strength of carbonated mortars was substantially higher than that of uncarbonated mortars. The flexural strength of the 1.0 M mix after 28 days of accelerated carbonation was 4.50 MPa (~185% higher than the maximum value reported for the uncarbonated mix—1.58 MPa). This increase was 28% for the 0.5 M mix.

For the 0.0 M mix, the flexural strength after 28 days of carbonation was similar to the maximum value (182 days) reported for the uncarbonated mix (10.12 and 10.68 MPa, respectively). It can be concluded that, as occurs in compressive strength, the highest relative increase in flexural strength due to carbonation takes place for the mixes with the highest proportions of MIBA, as it is a precursor with relatively high calcium content, where CO_2 reacts directly with C-A-S-H gel producing CaCO_3 [69].

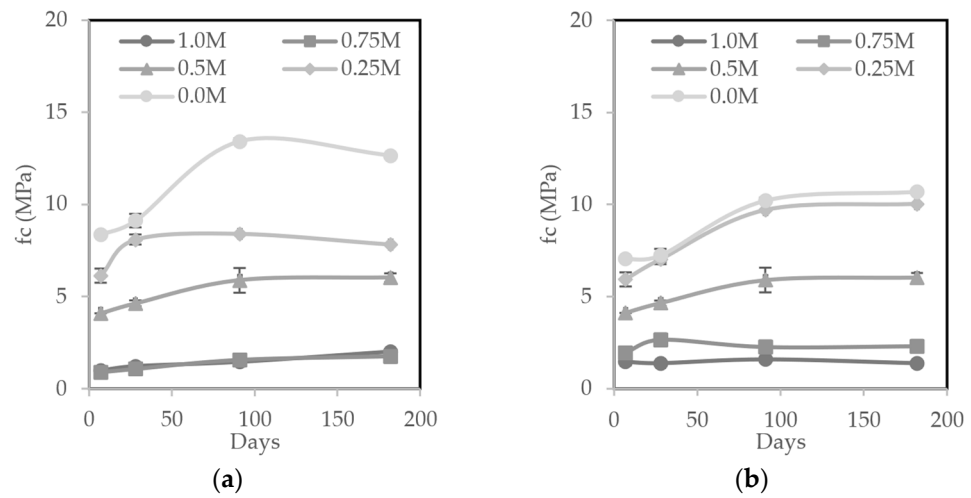


Figure 10. Flexural strength of: (a) OAA mortars and (b) CAA mortars.

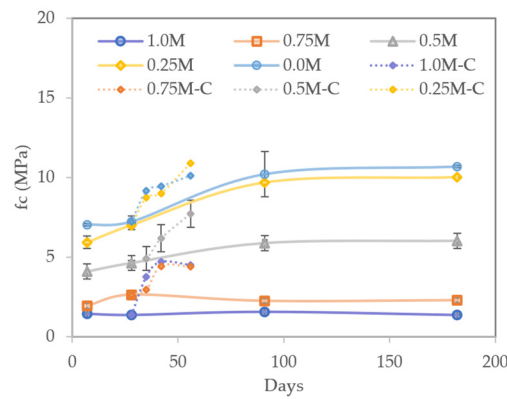


Figure 11. Flexural strength of uncarbonated and carbonated mortars with CAA design.

3.5.3. Dynamic Modulus of Elasticity

Figure 12 shows the results of the dynamic modulus of elasticity at 7, 28, 91, and 182 days for the mortars made with the OAA and the CAA designs. The maximum dynamic modulus of elasticity obtained for each alkaline activator design at 28 days corresponds to the mix with 100% FA: 28.1 and 24.9 GPa for the OAA and CAA designs, respectively. The minimum values correspond to the mix with 75% MIBA (i.e., 4.96 GPa) using an OAA design and 100% MIBA (i.e., 4.44 GPa) with a CAA design. This trend was maintained for longer curing times.

The dynamic modulus of elasticity is directly influenced by the porosity/density, cohesion of particles, and the presence of microcracks in the hardened material. Given the characteristics of MIBA, it was expected that prismatic specimens with a higher content of this precursor would present a lower dynamic modulus of elasticity. The opposite occurred for the mixes that contained a greater amount of FA (0.25 M and 0.0 M). These AAM presented a dynamic modulus of elasticity greater than 20 GPa after 28 days. This result is in accordance with that reported by Fernandez-Jimenez et al. [64], who obtained an average value of 17.1 GPa for the static modulus of elasticity at 28 days for alkali-activated concrete with FA as precursor and a mix of NaOH and Na₂SiO₃ as alkaline activator.

Figure 13 shows the linear correlation between the modulus of elasticity and the compressive strength for the OAA design (Figure 13a) and the CAA design (Figure 13b) mixes. The R² obtained at 28 days corresponds to 0.98 and 0.97 respectively, showing that there is a clear linear relationship between these two properties and little change with variation in the curing periods.

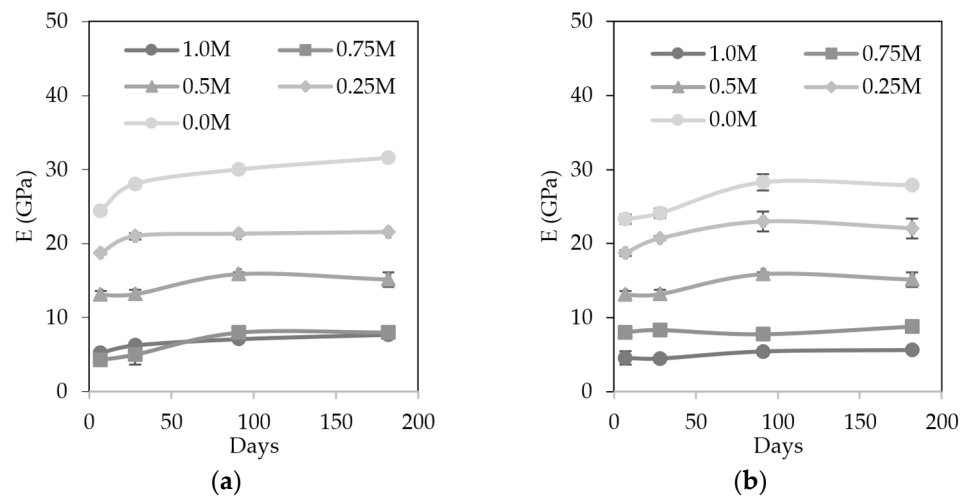


Figure 12. Dynamic modulus of elasticity of: (a) OAA mortars and (b) CAA mortars.

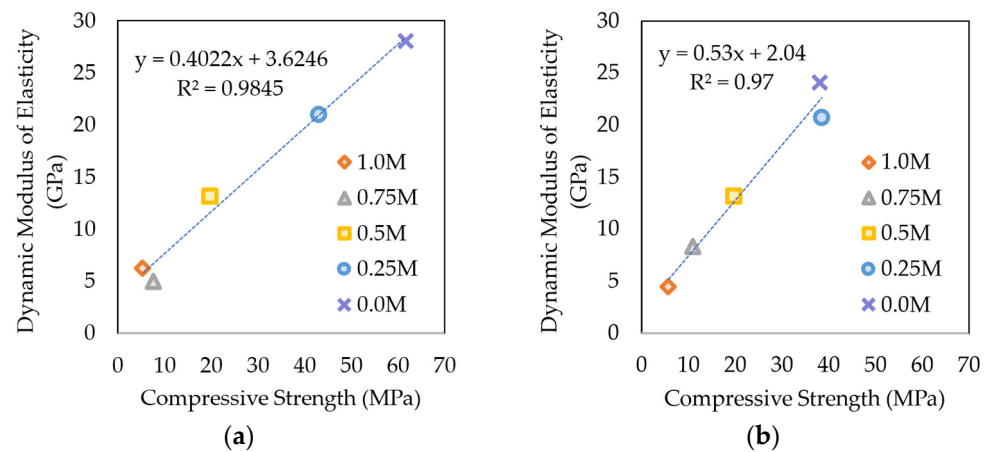


Figure 13. Correlation between the dynamic modulus of elasticity and compressive strength for: (a) OAA mortars and (b) CAA mortars.

3.5.4. Shrinkage

Figure 14 shows the results of the shrinkage test carried out on mortars with the CAA design. Measurements were made on sealed and unsealed mortars to evaluate the autogenous shrinkage. Shrinkage, in both cases, increased with increasing MIBA content. The highest shrinkage occurred at 115 days for mortars made with 100% MIBA (1600 and 1300 $\mu\text{m}/\text{m}$ for sealed and unsealed specimens, respectively).

Mixes with MIBA contents greater than 50% present curves that are very close to each other, whereas the mixes with 75% or 100% FA have a different behavior, constituting another group. Carvalho et al. [17] reported in their research that MIBA presents a morphology of irregular particles and porous microstructure. Shrinkage is directly influenced by the interconnected porosity of the material [22]. It is possible that, for MIBA percentages greater than 50%, the pre-treatment was not entirely effective. This may have resulted in a remnant of unreacted metallic aluminum particles, which led to damaging foaming reactions when in contact with Na_2SiO_3 , thereby increasing the specimens' porosity. Moreover, all mortars were exposed to thermal curing for 24 h, which accelerates water evaporation during the setting stage. This rapid water loss may have led to the formation of microcracks in the specimens that may have led to great shrinkage [61].

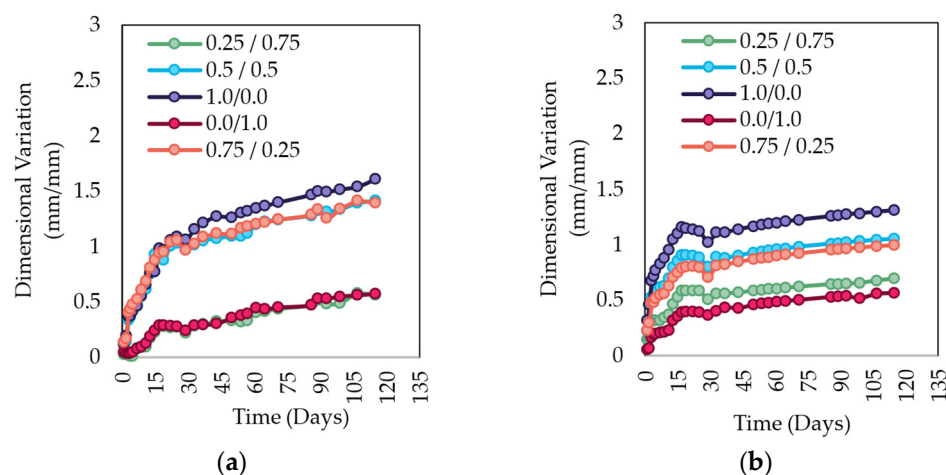


Figure 14. Shrinkage of the mortars using CAA design with (a) sealed or (b) unsealed curing.

The shrinkage of sealed specimens made with cement is usually lower than that of unsealed specimens, due to the greater water loss of the latter. In this case, the opposite was observed and was most likely due to the existence of the thermal curing stage, which significantly reduced the water content of the specimens. Sealed specimens, which have minimal exchange of water with the environment, exhibited shrinkage associated with the internal reactions within the AAM matrix, where a major consumption of internal water occurred. On the other hand, unsealed mortar specimens, after their thermal activation and throughout the curing process, were in a ~60% RH environment. This allowed for gas exchange, causing the increase in humidity of the specimens towards an equilibrium in the water vapor concentration with that of the external environment. Naturally, this led to hydration of the AAM matrix, offsetting the shrinkage caused by the internal reactions.

Yang et al. [71] studied the autogenous shrinkage of alkali-activated materials sealed with a polyethylene film, concluding that the storage conditions influence shrinkage. However, in the case of AAMs, autogenous shrinkage cannot be explained by the same theory as that of cement autogenous shrinkage, since there is a direct dependence between shrinkage and relative humidity [72].

3.5.5. Water Absorption by Capillary Action

The water absorption by capillary action test was carried out solely on the mixes with the CAA design in order to eliminate the influence of the $\text{SiO}_2/\text{Na}_2\text{O}$ and $\text{Na}_2\text{O}/\text{binder}$ variables. Figure 15 shows the results of capillary absorption coefficients in $\text{kg}/(\text{m}^2 \cdot \text{min}^{0.5})$ for each mix. Figure 15a corresponds to the coefficients obtained for the first stage of the test (measurements between 10 and 90 min), and Figure 15b corresponds to the coefficients calculated for the second stage of the test (measurements between 90 and 4320 min).

Figure 15b shows that the capillary coefficient was similar for mixes with MIBA contents equal to and below 50%, increasing remarkably for higher MIBA contents. The results are somewhat in accordance with the previous ones for other properties, again suggesting that the mortars with greater amounts of MIBA are more porous and, therefore, more susceptible to water movement. It should be noted that the capillarity coefficients obtained for 1.0 M mortars are not shown, since these mortars presented considerable mass loss during the test. In spite of the apparent unaffected exterior, it is possible that other MIBA-containing samples may also have presented some degree of mass loss influencing the water absorption coefficients.

Researchers on the matter have expressed different points of view regarding the role of the alkali (i.e., Na^+ in the present work) in the chemical structure of the oligomers formed. The poor physicochemical properties of some AAM are associated with the fact that the Na^+ ion is located at the borders of the cyclic oligomers, which means that it easily migrates to the surface in contact with water [73]. The opposite may occur when

the chemical structure formed is a three-dimensional network, where the Na^+ ion is fixed and trapped within the framework. Conversely, the results of other studies [74–76] have shown that some chemical bridges of Ca^{2+} in C-A-S-H are replaced with Na^+ , giving rise to C-(N)-A-S-H when using precursors such as blast furnace slag, which has a high Ca^{2+} content.

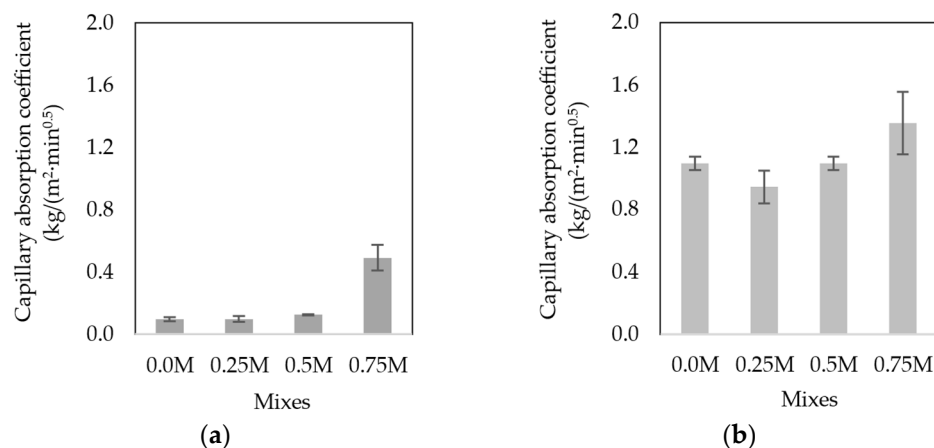


Figure 15. Capillary absorption coefficients of CAA mortars: (a) between 10 and 90 min; and (b) between 90 and 4320 min.

The results of the capillarity test indicate that, for the precursor rich in Ca^{2+} (i.e., MIBA) and the precursor low in Ca^{2+} (i.e., FA), Na^+ dissolves and leaches out of the mortars when water enters the capillaries, which indicates that a given amount of alkali is not physically bound within the matrix. This phenomenon was more noticeable in the specimens with a higher MIBA content, where the migration of excess Na^+ towards the surface gives rise to the precipitation of products (e.g., efflorescence of sodium carbonate).

3.5.6. Water Absorption by Immersion

Table 4 shows the results of the water absorption by immersion. Similar to the mechanical and durability properties, the percentage of water absorption increases with increasing MIBA content, despite presenting a similar value for the mixtures 0.0 M and 0.25 M.

Table 4. Water absorption by immersion of the mortars with the CAA design.

Mix	Water Absorption by Immersion (%)	Standard Deviation
0.0 M	13.4	0.14
0.25 M	13.1	0.09
0.5 M	14.8	0.30

It was not possible to obtain results for the 0.75 M and 1.0 M mixes, since the specimens broke 24 h after being submerged due to excessive loss of mass. This result confirms what was previously mentioned regarding the reaction products formed from the mixes, and the low content of amorphous phases present in the MIBA precursor.

4. Conclusions

From the above results, it is possible to conclude that:

- The chemical and mineralogical characterization of MIBA showed that it has potential to be activated, but the high aluminum content is problematic in alkali-activated materials due to the formation of hydrogen gas.
- The pre-treatment was effective at reducing the amount of pure aluminum available to react, thereby allowing the production of mortars with adequate dimensional stability;

- FA improved the workability of mixes in the fresh state, regardless of the activator design. Nonetheless, the mixes with the CAA design presented a higher fluidity since they had the lowest sodium silicate content;
- MIBA led to a less dense material due to the foaming reaction between the residual aluminum with the alkaline activator. This caused a higher porosity, lower mechanical strength, and higher water absorption, especially in contents equal to or greater than 75%. However, mixes with a maximum of 50% MIBA content did not show an excessive deterioration in the properties evaluated;
- Carbonation substantially improved the mechanical properties of AAM, especially in those with higher contents of MIBA, as it is a precursor with a high calcium content;
- Shrinkage of the sealed and unsealed specimens is influenced by thermal curing and storage conditions; therefore, the sealed specimens that experienced minimal exchange of water with the environment exhibited higher shrinkage associated with the internal reactions within the AAM matrix;
- All mixes presented sodium migration when performing the capillary test, the magnitude of which was greater in mixes with a greater amount of MIBA.

Author Contributions: Conceptualization, R.V.S.; methodology, R.V.S.; formal analysis, Y.A.; investigation, Y.A.; resources, R.V.S.; writing—original draft preparation, Y.A.; writing—review and editing, R.V.S. and J.d.B.; supervision, R.V.S. and J.d.B.; project administration, R.V.S.; funding acquisition, R.V.S. All authors have read and agreed to the published version of the manuscript.

Funding: This research was funded by FCT—Foundation for Science and Technology, through research projects PTDC/ECI-CON/29196/2017 (RIInoPolyCrete) and EXPL/ECI-EGC/0288/2021 (ECO₂Alkcrete).

Institutional Review Board Statement: Not applicable.

Informed Consent Statement: Not applicable.

Data Availability Statement: Not applicable.

Acknowledgments: The authors acknowledge the support of the CERIS Research Institute, IST, University of Lisbon.

Conflicts of Interest: The authors declare no conflict of interest.

References

1. International Labor Organization. Compilation of Decisions of the Committee. 2018. Available online: http://ilo.org/dyn/normlex/en/f?p=NORMLEXPUB:70002:0::NO::P70002_HIER_ELEMENT_ID,P70002_HIER_LEVEL:3945366,1 (accessed on 16 November 2021).
2. Stevano, S.; Ali, R.; Jamieson, M. Essential for what? A global social reproduction view on the re-organisation of work during the COVID-19 pandemic. *Can. J. Dev. Stud./Rev. Can. D'études Dév.* **2021**, *42*, 178–199. [[CrossRef](#)]
3. Wong, S.; Mah, A.X.Y.; Nordin, A.H.; Nyakuma, B.B.; Ngadi, N.; Mat, R.; Amin, N.A.S.; Ho, W.S.; Lee, T.H. Emerging trends in municipal solid waste incineration ashes research: A bibliometric analysis from 1994 to 2018. *Environ. Sci. Pollut. Res.* **2020**, *27*, 7757–7784. [[CrossRef](#)] [[PubMed](#)]
4. Explained Eurostat. Municipal Waste Statistic. Available online: https://ec.europa.eu/eurostat/statistics-explained/index.php?title=File:Municipal_waste_landfilled,_incinerated,_recycled_and_composted,_EU-28,_1995-017.png (accessed on 7 July 2021).
5. Explained Eurostat. Working from Home across EU Regions in 2020. Available online: <https://ec.europa.eu/eurostat/web/products-eurostat-news/-/ddn-20210923-1> (accessed on 25 September 2021).
6. Zhang, Y.; Wang, L.; Chen, L.; Ma, B.; Zhang, Y.; Ni, W.; Tsang, D.C.W. Treatment of municipal solid waste incineration fly ash: State-of-the-art technologies and future perspectives. *J. Hazard. Mater.* **2021**, *411*, 125132. [[CrossRef](#)] [[PubMed](#)]
7. Tang, P. Municipal Solid Waste Incineration (MSWI) Bottom Ash—From Waste to Value: Characterization, Treatments, and Application. Ph.D. Thesis, Eindhoven University of Technology, Eindhoven, The Netherlands, 2017.
8. Simões, B.; da Silva, P.; Silva, R.; Avila, Y.; Forero, J. Ternary mixes of self-compacting concrete with fly ash and municipal solid waste incinerator bottom ash. *Appl. Sci.* **2021**, *11*, 107. [[CrossRef](#)]
9. Clavier, K.A.; Paris, J.M.; Ferraro, C.C.; Townsend, T.G. Opportunities and challenges associated with using municipal waste incineration ash as a raw ingredient in cement production—A review. *Resour. Conserv. Recycl.* **2020**, *160*, 104888. [[CrossRef](#)]

10. Birgisdottir, H.; Bhandar, G.; Hauschild, M.Z.; Christensen, T.H. Life cycle assessment of disposal of residues from municipal solid waste incineration: Recycling of bottom ash in road construction or landfilling in Denmark evaluated in the ROAD-RES model. *Waste Manag.* **2007**, *27*, S75–S84. [[CrossRef](#)]
11. Keppert, M.; Pavlík, Z.; Tydlitát, V.; Volfová, P.; Švarcová, S.; Šyc, M.; Černý, R. Properties of municipal solid waste incineration ashes with respect to their separation temperature. *Waste Manag. Res.* **2012**, *30*, 1041–1048. [[CrossRef](#)]
12. Nodehi, M.; Taghvaei, V.M. Alkali-activated materials and geopolymer: A review of common precursors and activators addressing circular economy. *Circ. Econ. Sustain.* **2022**, *2*, 165–196. [[CrossRef](#)]
13. Gökçe, H.S.; Tuyan, M.; Nehdi, M.L. Alkali-activated and geopolymer materials developed using innovative manufacturing techniques: A critical review. *Constr. Build. Mater.* **2021**, *303*, 124483. [[CrossRef](#)]
14. Puertas, F.; Amat, T.; Fernández-Jiménez, A.; Vázquez, T. Mechanical and durable behaviour of alkaline cement mortars reinforced with polypropylene fibres. *Cem. Concr. Res.* **2003**, *33*, 2031–2036. [[CrossRef](#)]
15. Duxson, P.; Fernández-Jiménez, A.; Provis, J.L.; Lukey, G.C.; Palomo, A.; van Deventer, J.S. Geopolymer technology: The current state of the art. *J. Mater. Sci.* **2007**, *42*, 2917–2933. [[CrossRef](#)]
16. Casanova, S.; Silva, R.V.; de Brito, J.; Pereira, M.F.C. Mortars with alkali-activated municipal solid waste incinerator bottom ash and fine recycled aggregates. *J. Clean. Prod.* **2021**, *289*, 125707. [[CrossRef](#)]
17. Carvalho, R.; Silva, R.V.; de Brito, J.; Pereira, M.F.C. Alkali activation of bottom ash from municipal solid waste incineration: Optimization of NaOH- and Na₂SiO₃-based activators. *J. Clean. Prod.* **2021**, *291*, 125930. [[CrossRef](#)]
18. Alderete, N.M.; Joseph, A.M.; Van den Heede, P.; Matthys, S.; De Belie, N. Effective and sustainable use of municipal solid waste incineration bottom ash in concrete regarding strength and durability. *Resour. Conserv. Recycl.* **2021**, *167*, 105356. [[CrossRef](#)]
19. Wang, H.-W.; Chung, H.-W.; Teng, H.-T.; Cao, G. Generation of hydrogen from aluminum and water—effect of metal oxide nanocrystals and water quality. *Int. J. Hydrogen Energy* **2011**, *36*, 15136–15144. [[CrossRef](#)]
20. Luan, C.; Shi, X.; Zhang, K.; Utashev, N.; Yang, F.; Dai, J.; Wang, Q. A mix design method of fly ash geopolymer concrete based on factors analysis. *Constr. Build. Mater.* **2021**, *272*, 121612. [[CrossRef](#)]
21. Cho, Y.K.; Yoo, S.W.; Jung, S.H.; Lee, K.M.; Kwon, S.J. Effect of Na₂O content, SiO₂/Na₂O molar ratio, and curing conditions on the compressive strength of FA-based geopolymer. *Constr. Build. Mater.* **2017**, *145*, 253–260. [[CrossRef](#)]
22. Kuenzel, C.; Vandeperre, L.J.; Donatello, S.; Boccaccini, A.R.; Cheeseman, C. Ambient temperature drying shrinkage and cracking in metakaolin-based geopolymers. *J. Am. Ceram. Soc.* **2012**, *95*, 3270–3277. [[CrossRef](#)]
23. Rocha, T.D.; Dias, D.P.; Franca, F.C.C.; Guerra, R.R.D.; Marques, L. Metakaolin-based geopolymer mortars with different alkaline activators (Na⁺ and K⁺). *Constr. Build. Mater.* **2018**, *178*, 453–461. [[CrossRef](#)]
24. Mary Joseph, A.; Snellings, R.; Nielsen, P.; Matthys, S.; De Belie, N. Pre-treatment and utilisation of municipal solid waste incineration bottom ashes towards a circular economy. *Constr. Build. Mater.* **2020**, *260*, 120485. [[CrossRef](#)]
25. Huang, G.; Yang, K.; Sun, Y.; Lu, Z.; Zhang, X.; Zuo, L.; Feng, Y.; Qian, R.; Qi, Y.; Ji, Y.; et al. Influence of NaOH content on the alkali conversion mechanism in MSWI bottom ash alkali-activated mortars. *Constr. Build. Mater.* **2020**, *248*, 118582. [[CrossRef](#)]
26. Maldonado-Alameda, A.; Mañosa, J.; Giro-Paloma, J.; Formosa, J.; Chimenos, J.M. Alkali-activated binders using bottom ash from waste-to-energy plants and aluminium recycling waste. *Appl. Sci.* **2021**, *11*, 3840. [[CrossRef](#)]
27. Cristelo, N.; Segadães, L.; Coelho, J.; Chaves, B.; Sousa, N.R.; de Lurdes Lopes, M. Recycling municipal solid waste incineration slag and fly ash as precursors in low-range alkaline cements. *Waste Manag.* **2020**, *104*, 60–73. [[CrossRef](#)] [[PubMed](#)]
28. Wongsa, A.; Boonserm, K.; Waisurasingha, C.; Sata, V.; Chindaprasirt, P. Use of municipal solid waste incinerator (MSWI) bottom ash in high calcium fly ash geopolymer matrix. *J. Clean. Prod.* **2017**, *148*, 49–59. [[CrossRef](#)]
29. Huang, G.; Yang, K.; Chen, L.; Lu, Z.; Sun, Y.; Zhang, X.; Feng, Y.; Ji, Y.; Xu, Z. Use of pretreatment to prevent expansion and foaming in high-performance MSWI bottom ash alkali-activated mortars. *Constr. Build. Mater.* **2020**, *245*, 118471. [[CrossRef](#)]
30. Wang, C.; He, H.; Wang, Y.; Xue, W. Effects of fluorogypsum and flue-gas desulfurization gypsum on the hydration and hardened properties of alkali slag cement. *Crystals* **2021**, *11*, 1475. [[CrossRef](#)]
31. Yurt, Ü.; Bekar, F. Comparative study of hazelnut-shell biomass ash and metakaolin to improve the performance of alkali-activated concrete: A sustainable greener alternative. *Constr. Build. Mater.* **2022**, *320*, 126230. [[CrossRef](#)]
32. Lima, S.; Gomes, T.; Moraes, J. Novel one-part alkali-activated binder produced with coffee husk ash. *Mater. Lett.* **2022**, *313*, 131733. [[CrossRef](#)]
33. European Council. Council Directive 98/83/EC of 3 November 1998 on the quality of water intended for human consumption. *Off. J. Eur. Communities* **1998**, *330*, 32–54.
34. Topçu, İ.; Ateşin, Ö. Effect of high dosage lignosulphonate and naphthalene sulphonate based plasticizer usage on micro concrete properties. *Constr. Build. Mater.* **2016**, *120*, 189–197. [[CrossRef](#)]
35. EN 12620; Aggregates for Concrete. Comité Européen de Normalisation (CEN): Brussels, Belgium, 2002.
36. Rosenband, V.; Gany, A. Application of activated aluminum powder for generation of hydrogen from water. *Int. J. Hydrogen Energy* **2010**, *35*, 10898–10904. [[CrossRef](#)]
37. EN-196-1; Methods of Testing Cement—Part 1: Determination of Strength. Comité Européen de Normalisation (CEN): Brussels, Belgium, 2005; 36p.
38. ASTM D4972; Standard Test Methods for pH of Soils. American Society for Testing and Materials: West Conshohocken, PA, USA, 2019.
39. EN-933-1; Tests for Geometrical Properties of Aggregates—Part 1: Determination of Particle Size Distribution. Sieving Method. Comité Européen de Normalisation (CEN): Brussels, Belgium, 2012; 22p.

40. EN-1097-6; Tests for Mechanical and Physical Properties of Aggregates—Part 6: Determination of Particle Density and Water Absorption. Comité Européen de Normalisation (CEN): Brussels, Belgium, 2013; 54p.
41. EN-1015-3; Methods of Test for Mortar for Masonry—Part 3: Determination of Consistence of Fresh Mortar (By Flow Table). Comité Européen de Normalisation (CEN): Brussels, Belgium, 1999; 10p.
42. EN-1015-6; Methods of Test for Mortar for Masonry—Part 6: Determination of Bulk Density of Fresh Mortar. Comité Européen de Normalisation (CEN): Brussels, Belgium, 1999; 8p.
43. EN 1015-11; Determination of Flexural and Compressive Strength of Hardened Mortar. Comité Européen de Normalisation (CEN): Brussels, Belgium, 1999.
44. EN-1015-10; Methods of Test for Mortar for Masonry—Part 10: Determination of Dry Bulk Density of Hardened Mortar. Comité Européen de Normalisation (CEN): Brussels, Belgium, 1999; 10p.
45. EN 14146; Natural Stone Test Methods. Determination of the Dynamic Elastic Modulus of Elasticity (By Measuring the Fundamental Resonance Frequency). Comité Européen de Normalisation (CEN): Brussels, Belgium, 2004; 18p.
46. EN-1015-13; Methods of Test for Mortar for Masonry—Part 13: Determination of Dimensional Stability of Hardened Mortars. Comité Européen de Normalisation (CEN): Brussels, Belgium, 1993; 20p.
47. EN-1015-18; Methods of Test for Mortar for Masonry—Part 18: Determination of Water Absorption Coefficient Due to Capillary action of Hardened Mortar. Comité Européen de Normalisation (CEN): Brussels, Belgium, 2002; 12p.
48. LNEC-E394; Concrete: Determination of Water Absorption by Immersion—Testing at Atmospheric Pressure (in Portuguese). National Laboratory in Civil Engineering (LNEC—Laboratório Nacional de Engenharia Civil): Lisbon, Portugal, 1993; 2p.
49. EN-13295; Products and Systems for the Protection and Repair of Concrete Structures. Test Methods. Determination of Resistance To Carbonation. Comité Européen de Normalisation (CEN): Brussels, Belgium, 2004; 18p.
50. ASTM C618; Standard Specification for Coal Fly Ash and Raw or Calcined Natural Pozzolan for Use in Concrete. American Society for Testing and Materials: West Conshohocken, PA, USA, 2019.
51. Lynn, C.J.; Dhir, R.K.; Ghataora, G.S. Municipal incinerated bottom ash use as a cement component in concrete. *Mag. Concr. Res.* **2017**, *69*, 512–525. [[CrossRef](#)]
52. Wei, Y.; Saffarzadeh, A.; Shimaoka, T.; Zhao, C.; Peng, X.; Gao, J. Geoenvironmental weathering/deterioration of landfilled MSWI-BA glass. *J. Hazard. Mater.* **2014**, *278*, 610–619. [[CrossRef](#)]
53. Bayuseno, A.P.; Schmahl, W.W. Understanding the chemical and mineralogical properties of the inorganic portion of MSWI bottom ash. *Waste Manag.* **2010**, *30*, 1509–1520. [[CrossRef](#)] [[PubMed](#)]
54. Rashad, A.M.; Zeedan, S.R. The effect of activator concentration on the residual strength of alkali-activated fly ash pastes subjected to thermal load. *Constr. Build. Mater.* **2011**, *25*, 3098–3107. [[CrossRef](#)]
55. Engineering ToolBox. Hydrogen—Density and Specific Weight. 2018. Available online: https://www.engineeringtoolbox.com/hydrogen-H2-density-specific-weight-temperature-pressure-_2044.html (accessed on 17 July 2019).
56. Das, S.K.; Mustakim, S.M.; Adesina, A.; Mishra, J.; Alomayri, T.S.; Assaedi, H.S.; Kaze, C.R. Fresh, strength and microstructure properties of geopolymer concrete incorporating lime and silica fume as replacement of fly ash. *J. Build. Eng.* **2020**, *32*, 101780. [[CrossRef](#)]
57. Kuri, J.; Khan, M.; Sarker, P. Fresh and hardened properties of geopolymer binder using ground high magnesium ferronickel slag with fly ash. *Constr. Build. Mater.* **2021**, *272*, 121877. [[CrossRef](#)]
58. Provis, J.L.; Duxson, P.; van Deventer, J.S. The role of particle technology in developing sustainable construction materials. *Adv. Powder Technol.* **2010**, *21*, 2–7. [[CrossRef](#)]
59. Kujawa, W.; Olewnik-Kruszkowska, E.; Nowaczyk, J. Concrete strengthening by introducing polymer-based additives into the cement matrix—A mini review. *Materials* **2021**, *14*, 6071. [[CrossRef](#)]
60. Burgos-Montes, O.; Palacios, M.; Rivilla, P.; Puertas, F. Compatibility between superplasticizer admixtures and cements with mineral additions. *Constr. Build. Mater.* **2012**, *31*, 300–309. [[CrossRef](#)]
61. Eliche-Quesada, D.; Ruiz-Molina, S.; Pérez-Villarejo, L.; Castro, E.; Sánchez-Soto, P.J. Dust filter of secondary aluminium industry as raw material of geopolymer foams. *J. Build. Eng.* **2020**, *32*, 101656. [[CrossRef](#)]
62. Provis, J.L.; Fernández-Jiménez, A.; Kamseu, E.; Leonelli, C.; Palomo, A. Binder chemistry—Low-calcium alkali-activated materials. In *Alkali Activated Materials*; Provis, J.L., van Deventer, J.S.J., Eds.; Springer: Berlin/Heidelberg, Germany, 2014; pp. 93–123.
63. Bernal, S.A.; Provis, J.L.; Fernández-Jiménez, A.; Krivenko, P.V.; Kavalerova, E.; Palacios, M.; Shi, C. Binder chemistry—high-calcium alkali-activated materials. In *Alkali Activated Materials*; Provis, J.L., van Deventer, J.S.J., Eds.; Springer: Berlin/Heidelberg, Germany, 2014; pp. 59–91.
64. Fernandez-Jimenez, A.; Palomo, A.; Lopez-Hombrados, C. Engineering properties of alkali-activated fly ash concrete. *ACI Mater. J.* **2006**, *103*, 106.
65. Duxson, P.; Mallicoat, S.; Lukey, G.; Kriven, W.; van Deventer, J. The effect of alkali and Si/Al ratio on the development of mechanical properties of metakaolin-based geopolymers. *Colloids Surf. A Physicochem. Eng. Asp.* **2007**, *292*, 8–20. [[CrossRef](#)]
66. Khalid, H.; Lee, N.; Choudhry, I.; Wang, Z.; Lee, H.K. Evolution of zeolite crystals in geopolymer-supported zeolites: Effects of composition of starting materials. *Mater. Lett.* **2019**, *239*, 33–36. [[CrossRef](#)]
67. Moudar, J.; El Fami, N.; Diouri, A.; Taibi, M. Identification and characterization of faujasite zeolite phase in alkali activated class F fly ash. *Mater. Today Proc.* **2022**. [[CrossRef](#)]

68. Xie, J.; Wang, J.; Rao, R.; Wang, C.; Fang, C. Effects of combined usage of GGBS and fly ash on workability and mechanical properties of alkali activated geopolymer concrete with recycled aggregate. *Compos. Part B Eng.* **2019**, *164*, 179–190. [[CrossRef](#)]
69. Zhang, P.; Gao, Z.; Wang, J.; Guo, J.; Hu, S.; Ling, Y. Properties of fresh and hardened fly ash/slag based geopolymer concrete: A review. *J. Clean. Prod.* **2020**, *270*, 122389. [[CrossRef](#)]
70. Huang, G.; Ji, Y.; Li, J.; Hou, Z.; Jin, C. Use of slaked lime and Portland cement to improve the resistance of MSWI bottom ash-GBFS geopolymer concrete against carbonation. *Constr. Build. Mater.* **2018**, *166*, 290–300. [[CrossRef](#)]
71. Yang, T.; Zhu, H.; Zhang, Z. Influence of fly ash on the pore structure and shrinkage characteristics of metakaolin-based geopolymer pastes and mortars. *Constr. Build. Mater.* **2017**, *153*, 284–293. [[CrossRef](#)]
72. Archez, J.; Farges, R.; Gharzouni, A.; Rossignol, S. Influence of the geopolymer formulation on the endogeneous shrinkage. *Constr. Build. Mater.* **2021**, *298*, 123813. [[CrossRef](#)]
73. Davidovits, J. *Geopolymer Chemistry and Applications*, 5th ed.; Geopolymer Institute: Saint-Quentin, France, 2008.
74. Haha, M.B.; Le Saout, G.; Winnefeld, F.; Lothenbach, B. Influence of activator type on hydration kinetics, hydrate assemblage and microstructural development of alkali activated blast-furnace slags. *Cem. Concr. Res.* **2011**, *41*, 301–310. [[CrossRef](#)]
75. San Nicolas, R.; Provis, J. Interfacial transition zone in alkali-activated slag concrete. In Proceedings of the 12th International Conference on Recent Advances in Concrete Technology and Sustainability Issues, Prague, Czech Republic, 30 October 2012.
76. Bernal, S.A.; San Nicolas, R.; Provis, J.L.; De Gutiérrez, R.M.; van Deventer, J.S. Natural carbonation of aged alkali-activated slag concretes. *Mater. Struct.* **2014**, *47*, 693–707. [[CrossRef](#)]